nature nanotechnology

Article

https://doi.org/10.1038/s41565-024-01773-4

Revealing the degradation pathways of layered Li-rich oxide cathodes

Received: 22 July 2023

Accepted: 24 July 2024

Published online: 02 September 2024

Check for updates

Zhimeng Liu[1,14], Yuqiang Zeng[2,3,14], Junyang Tan[4,14], Hailong Wang[1,2,14], Yudong Zhu[5], Xin Geng[1], Peter Guttmann[6], Xu Hou[7], Yang Yang[8,9], Yunkai Xu[10], Peter Cloetens[9], Dong Zhou[11], Yinping Wei[4], Jun Lu[10] ✉, Jie Li[7,12] ✉, Bilu Liu[4], Martin Winter[7], Robert Kostecki[3], Yuanjing Lin[2] ✉ & Xin He[1,13] ✉

Layered lithium-rich transition metal oxides are promising cathode candidates for high-energy-density lithium batteries due to the redox contributions from transition metal cations and oxygen anions. However, their practical application is hindered by gradual capacity fading and voltage decay. Although oxygen loss and phase transformation are recognized as primary factors, the structural deterioration, chemical rearrangement, kinetic and thermodynamic effects remain unclear. Here we integrate analysis of morphological, structural and oxidation state evolution from individual atoms to secondary particles. By performing nanoscale to microscale characterizations, distinct structural change pathways associated with intraparticle heterogeneous reactions are identified. The high level of oxygen defects formed throughout the particle by slow electrochemical activation triggers progressive phase transformation and the formation of nanovoids. Ultrafast lithium (de)intercalation leads to oxygen-distortion-dominated lattice displacement, transition metal ion dissolution and lithium site variation. These inhomogeneous and irreversible structural changes are responsible for the low initial Coulombic efficiency, and ongoing particle cracking and expansion in the subsequent cycles.

Layered lithium-rich transition metal oxide (LRTMO) materials are regarded as promising high-energy cathodes due to the redox of both transition metal (TM) cations and oxygen anions[1–4]. However, the performance of LRTMOs is limited by oxygen release, the sluggish kinetics of anionic redox, and non-equilibrium lithium-ion diffusion[5]. In addition, lattice displacement and nanostrain evolution lead to irreversible structural changes during the electrochemical redox processes[6], resulting in voltage decay and disruption of lithium-ion transport pathways, further exacerbating the dynamic sluggishness[7]. Although previous research has revealed that the degradation of LRTMOs is closely related to the inherent thermodynamic instability of the host structure[8], the degradation details throughout the particle remain elusive, particularly for localized nanoscale domains.

Because both TM cations and oxygen anions play critical roles in electrochemical performance and structural degradation[9], an integrated analysis of these two redox centres is essential to elucidate the complex redox mechanism, along with information on particle heterogeneities that also strongly affect the degradation. Energy-resolved transmission X-ray microscopy (TXM) can provide computed phase-contrast tomography for comprehensive understanding of the local morphological and chemical mapping with three-dimensional (3D) spatial resolution[10], including heterogeneous oxidation of cations[11] or anions[12], cation rearrangement[13], chemical composition distribution[14,15], and propagation of nano- to microsized cracks[16]. However, it is challenging to integrate such a cation–anion redox-determined morphological, structural, chemical and oxidation state evolution analysis with the association of kinetic and thermodynamic effects.

In this work, we use TXM in the soft energy region and scanning transmission electron microscopy (STEM) with high-angle annular

A full list of affiliations appears at the end of the paper. ✉e-mail: junzoelu@zju.edu.cn; jie1.li@polimi.it; linyj2020@sustech.edu.cn; xinhe@scu.edu.cn

dark-field (HAADF) and integrated differential phase-contrast (iDPC) modes to systematically investigate the degradation heterogeneities from the intact particle down to the nanoscale region. Such an analysis of representative individual particles can yield a comprehensive understanding of the degradation mechanism during the electrochemical process. Our work identified distinct degradation pathways associated with different intraparticle heterogeneous reactions. The degradation of LRTMOs when cycled at low current rate originates from substantial oxygen-defect formation across the particle, which also releases oxygen and triggers progressive phase transformation from the surface into the bulk. However, the fast kinetics during ultrafast lithium (de)intercalation with heterogeneous lithium-ion diffusion leads to oxygen-distortion-dominated lattice displacement and is associated with TM-ion dissolution and lithium-site variation.

Electrochemical properties and atomic visualization

The electrochemical performance of an LRTMO ($Li_{1.2}Mn_{0.56}Ni_{0.16}Co_{0.08}O_2$) is shown in Fig. 1a,b. The oxygen loss at a low current rate (0.1 C) causes low initial Coulombic efficiency (ICE) and voltage decay during subsequent cycles. However, it is noteworthy that the fast kinetics at a high current rate (10 C) exacerbates initial irreversibility, amplifies overpotential and intensifies capacity fading. As shown in Fig. 1c,d, STEM-HAADF and STEM-iDPC images indicate that ordered atoms are uniformly distributed in TM–oxygen coordination with a well-organized layer structure in the pristine sample (Fig. 1e), and a lithium layer in the middle of oxygen slabs corresponds to typical octahedral sites. After 20 cycles at 0.1 C, a phase transformation from layer to spinel to rock-salt phase[17] on the surface is observed in Fig. 1f. Meanwhile, nanovoids, formed due to the generation of oxygen vacancies, are heterogeneously distributed as nanoscale dark areas in the bulk[18] (Fig. 1f), and the deficiency of oxygen in the nanovoids was demonstrated by electron energy loss spectroscopy (EELS) (Supplementary Fig. 15) and energy-dispersive spectroscopy (EDS) (Supplementary Fig. 16). Previous research has proven that oxidation of the O^{2-} anion lowers both the formation energy of oxygen vacancies and the migration barrier of oxidized oxygen[18], thereby providing the energetic driving force for oxygen gas release from the surface[19,20] and oxygen defect aggregation in the bulk (as shown in Fig. 1g). Nearly 4% of total oxygen loss occurs in the first cycle and remains at a consistent level after 20 cycles, as confirmed by neutron powder diffraction (NPD) and the refinement results shown in Supplementary Figs. 1–13 and 14c,d.

As the current increased to 10 C, the occurrence of nanoscale slab twisting and bending results in further distinct structural rearrangement patterns. In detail, the STEM-HAADF image shown in Fig. 1h demonstrates lattice distortion with varied interlayer distance along the *c* direction and confirmed the existence of a TM-deficient region (yellow dashed rectangle), which differs from the intermediate phase observed when rapidly charging $LiNi_{1/3}Mn_{1/3}Co_{1/3}O_2$ (ref. 21). This lattice distortion exists widely in the bulk of the particles cycled at 10 C (Supplementary Fig. 17). This could relate to the early stage of grain boundary formation induced by a highly strained lattice (see Supplementary Fig. 18 for geometrical phase analysis), which promotes crack propagation and TM dissolution[22]. The corresponding STEM-iDPC images (Fig. 1i–l) and schematic structure image (Fig. 1m) show that lattice displacement domains are randomly incorporated into the original layered framework while sharing the coherent structure. Details of the atomic configuration are shown in Fig. 1j–l: the positions of some oxygen anions and residual lithium ions within the dashed rectangles deviate from the original sites due to non-uniform lithium-ion diffusion, which indicates strong lattice distortion (Fig. 1m) and changes in Li_{oct} versus Li_{tet} occupation. Because the Li_{tet} is assumed to be energetically favourable[21], some lithium ions may be stabilized or trapped in these sites, thus impeding their diffusion capability[9,23]. As a result, a lower proportion of lithium ions can be reversibly inserted/extracted from the lithium layer in the host structure during rapid cycling (Supplementary Fig. 14a,b). The displacement of the oxygen position can be attributed to a large variation in the TM–oxygen bond length, which is manifested as large-scale slab twisting and bending (Fig. 1m). Such substantial lithium-ion diffusion heterogeneity and gradually accumulated nanoscale tensile strains have a great impact on the structural and chemical evolution, leading to different degradation pathways of LRTMOs. Operando X-ray diffraction (XRD) was performed to provide direct evidence of the different structural degradation mechanisms operating at different current rates (Supplementary Fig. 19). The position of the (003) peak undergoes continuous slow changes and there is a sharp increase in the lattice *c* dimension at 0.1 C and 10 C, respectively. These differences are attributed to rapid phase transition and lattice distortion caused by the inhomogeneity of lithium-ion deintercalation during rapid charging.

Visualization of morphology and chemical structure evolution

Synchrotron-based soft TXM was carried out to directly visualize the spatial morphological, chemical–structural and oxidation-state-related status of the sample particles at various voltages as circled in Fig. 1b. The coloured segments in 3D tomography and cross-sectional slices (Fig. 2a) represent the distribution of chemical species with various signatures, while the categorizing criteria are based on the quantification of the TM/oxygen ratio. For the pristine sample, 93.6% of the total bulk volume has the target composition, that is, the representative cross-sectional image through the 3D volume presumably suggests that a slight nanoscale deficiency of cations is only present on the surface, whereas similar behaviour could also be observed in the regular $LiNi_{1-x-y}Mn_xCo_yO_2$ material[10]. Moreover, the presence of randomly distributed red points on the surface indicates oxygen defects, which originate from the annealing process[24].

Under a charging current rate of 0.1 C, agglomerated oxygen-poor (red) segments initiate simultaneously from both surface and bulk when the voltage reaches to 4.6 V. These oxygen-poor segments have higher TM/oxygen ratios than the target composition, and this ratio depends strongly on the segment's location. These segments could be the result of oxygen defects remaining in the lattice arising from substantial oxygen release from the surface, and trapped oxygen in the bulk that may be involved in subsequent redox reactions[19] and be slowly released from the surrounding secondary structure[25]. The overall *c* lattice dimension (Supplementary Fig. 14e) first expands as lithium ions are extracted from the bulk, then starts to decrease because oxygen defects release lattice strain. Oxygen-loss domains continue accumulating in the high-voltage plateau, which is consistent with analysis of oxygen occupancy by NPD (Supplementary Fig. 14c) and mapping of resonant inelastic X-ray scattering (mRIXS) characterization[19,26,27]. At 4.8 V, a dramatic drop in *c* occurs due to the formation of substantial oxygen defects and TM dissolution (mainly manganese) or in-plane migration widely distributed throughout the particles (Fig. 2b) with reduced TM/oxygen ratios[20]. As lithium ions insert back, the proportion of oxygen-poor segments remains consistent with the fully charged state, suggesting that irreversible reactions mainly occur during the charging process and permanently change the structure and composition of LRTMOs. The oxygen redox behaviour is different at the surface and in the bulk: overoxidized oxygen at the surface is released as oxygen gas, while in the bulk it is trapped in oxygen defects. Although operando differential electrochemical mass spectrometry (DEMS) has confirmed that oxygen gas release mainly happens during the high-voltage plateau of the initial charging process[28], the distribution of oxygen defects in the particle and their corresponding activity have not been elucidated. Integrated spatial chemical composition analysis has identified the location of oxygen defects and provided insights into the structural evolution pathway. Most oxygen defects form by the end of the first charging process, releasing oxygen gas

https://doi.org/10.1038/s41565-024-01773-4

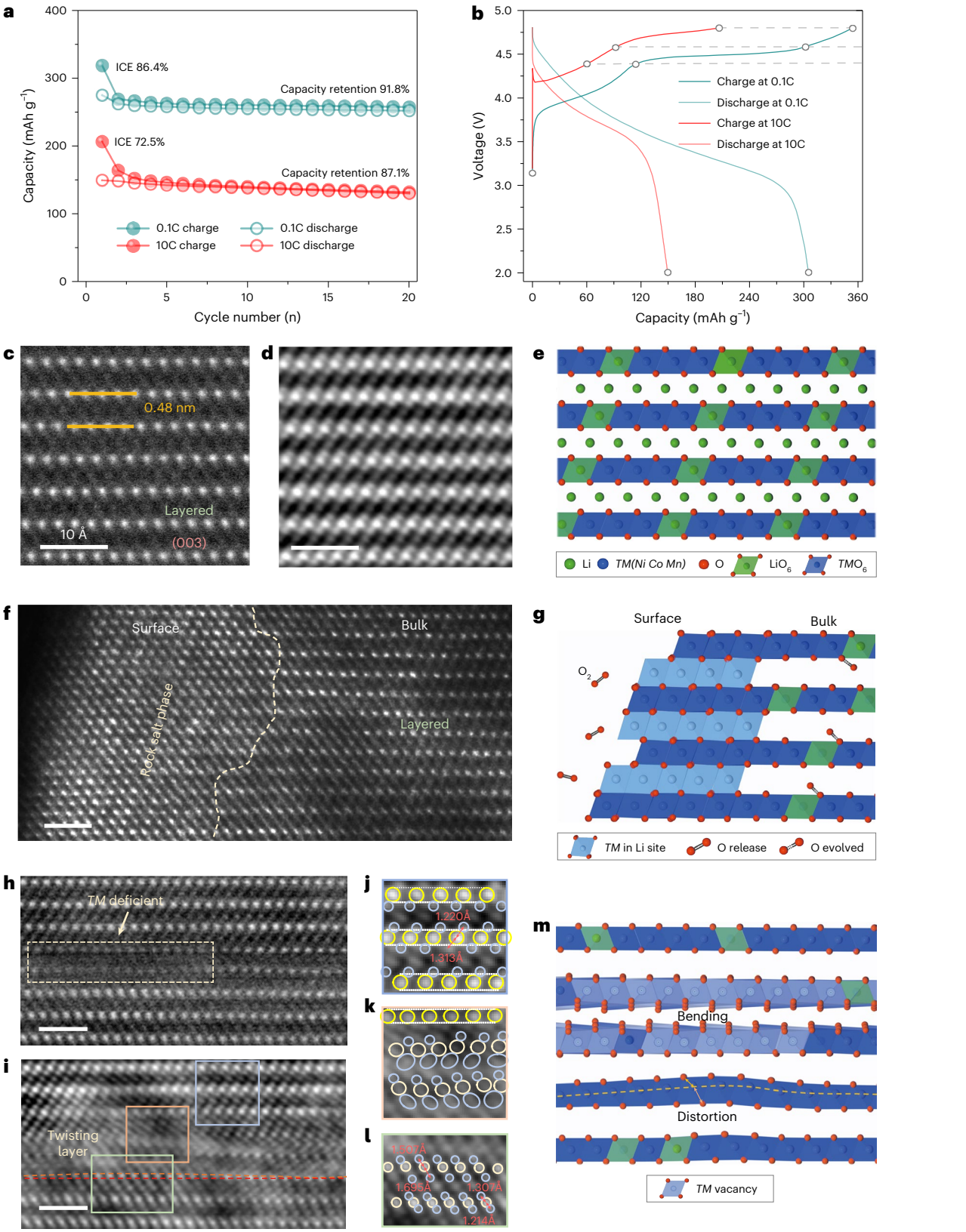

Fig. 1 | Electrochemical performance and lattice structure of LRTMO cathodes. a,**b**, The cycling profile (**a**) and first cycle charge–discharge curves (**b**) of LRTMO at current rates of 0.1 and 10 C. **c**–**e**, High-resolution STEM images and schematic structure showing the atomic arrangement of LRTMO in the pristine state: STEM-HAADF image (**c**) (nickel, manganese and cobalt atoms are heavy scatterers and appear white); the corresponding STEM-iDPC image with clearly visible oxygen atoms (**d**); and a schematic illustration of the crystal structure (**e**). **f**,**g**, STEM-HAADF image of LRTMO cycled at 0.1 C for 20 cycles (**f**) and a schematic structure (**g**) indicating that when going from surface to bulk the structure changes from rock salt to layered. **h**,**i**, STEM-HAADF image (**h**) and the corresponding STEM-iDPC image (**i**) of LRTMO cycled at 10 C for 20 cycles. **j**–**l**, The areas demarcated in **i** indicate the regular region marked with light blue (**j**), the TM-deficient region marked with orange (**k**) and the structurally twisted region marked with light green (**l**). **m**, Schematic structure with three representative domains corresponding to kinetic- and dynamic-effect-induced distortion.

https://doi.org/10.1038/s41565-024-01773-4

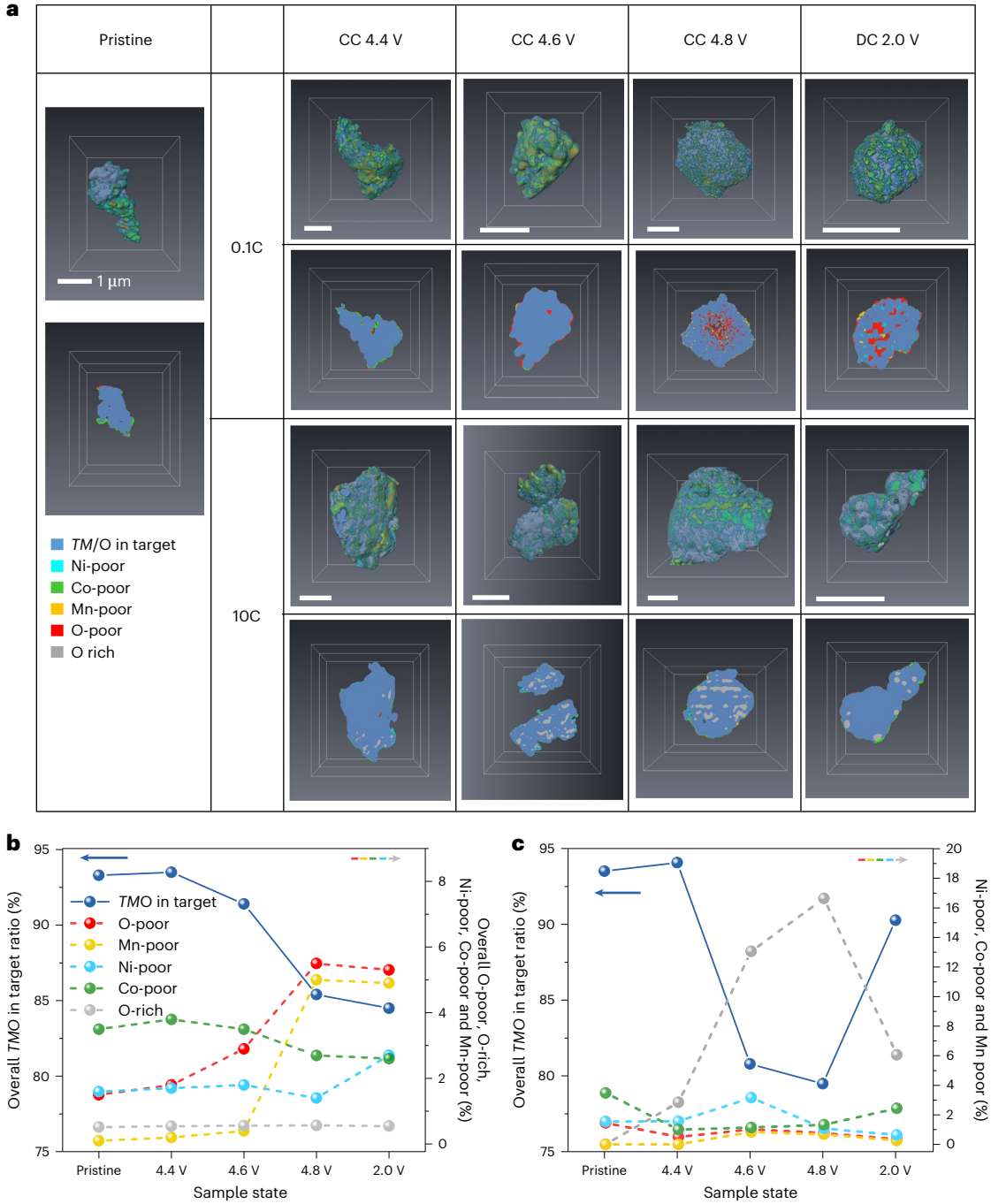

Fig. 2 | Elemental association evolution and principal component quantification. a, 3D rendering and randomly selected cross-sectional slices for the distribution of the elemental associations at representative cut-off voltages which were generated by soft TXM. The reconstructed images are achieved through computed correlation analysis of the absorption coefficient as a function of the X-ray energy (L-edges for TMs and K-edge for oxygen) within the imaged nanoscale area (Supplementary Table 1). Each colour bar represents a local elemental association as a function of the X-ray energy within the imaged nanoscale areas, which are shown at the bottom of the pristine sample. The 3D rendering includes each elemental association with merged colour; only the local elemental association with the highest proportion is apparent in the 2D slices. CC, charged state; DC, discharged state. **b**,**c**, Proportions of each elemental association through the particle for the electrode sample at different electrochemical stages of the 0.1 C group (**b**) and the 10 C group (**c**).

and triggering a phase transformation on the surface. However, some defects remain in the bulk and continue participating in the redox reaction during subsequent cycles. These locally diffused oxygen defects in the bulk gradually transform into nanovoids that penetrate into the deeper region of the particle[18], resulting in an ongoing expansion of the lattice structure with further cycles.

In contrast to the oxygen-loss-dominated structural evolution that occurs at 0.1 C, fast charging of the LRTMO induced highly inhomogeneous electrochemical kinetics and non-equilibrium ionic-diffusion dynamics, resulting in a distinctly different degradation pathway. The grey areas in Fig. 2a represent oxygen-rich segments, that is, a TMs/O ratio lower than target composition. This is possibly due to the combination of TM dissolution, oxygen distortion and lithium–oxygen sliding, as demonstrated in Fig. 1h,i. Although only a few oxygen-rich nanodomains appear at the subsurface when the voltage reaches 4.4 V, their presence indicates that lattice distortions have

already started to form due to the heterogeneous reactions, and may also relate to the existence of diffusive oxygen species (such as O_2^{2-} or O^- which are more mobile than O^{2-}). Inhomogeneous lithium-ion diffusion causes large overpotentials throughout the nanoscale particles, and is associated with the formation of oxygen-rich segments and lithium ions trapped in tetrahedral sites, hindering further lithium-ion diffusion. These findings provide solid evidence to support the conclusion that fast charging could lead to early activation of oxygen anions heterogeneously[9]. As the voltage is increased to 4.8 V, widely distributed nanoscale oxygen-rich domains become interconnected, forming large domains that occupy around 17% of the volume throughout the particle (Fig. 2c). The confined coherent lattice distortion gradually expands and then acquires cumulated tensile strain in the delithiated LRTMO, which corresponds to a higher *c* value without any oxygen release to reduce the lattice strain. The non-release of oxygen in the fast-charging process can be reasonably explained by the kinetic square scheme, whereby the kinetically sluggish O–O dimerization is inhibited during the fast-charging process, thus reducing the oxygen release due to further oxidation of O_2^{n-} to oxygen gas[29]. After complete lithiation, a portion of the oxygen-rich domains could return to their original composition. The recovery of oxygen-rich domains suggests that these are primarily caused by lattice distortion, and thus can be partly recovered by reversible lithiation. The existence of oxygen-rich domains may relate to the occurrence of irreversible TM dissolution, diffusion of oxygen species, and combined with displacement of residual oxygen. This phenomenon further influences the reversible lithiation process and has been quantified by NPD (Supplementary Fig. 14a). These results indicate that the degradation of fast-cycled LRTMO is determined by dynamically governed inhomogeneous lithium-ion diffusion and by the strain induced by regional lattice distortion.

Nanoprobing state-of-charge heterogeneity

By coupling full-field imaging with the function of energy tunability from the soft TXM scan (Supplementary Table 2), two-dimensional (2D) resolved spectroscopic signals with sufficient sensitivities are extracted from the corresponding measurements[30]. The colour distribution mapping shown in Fig. 3a represents the oxidation states of TM cations and oxygen anions, whereas the particles at representative states of charge (SOCs) are consistent with the analysis presented in Fig. 2. An inhomogeneous mixture of multivalence states for both manganese and nickel in the pristine particle could be attributed to the nanodomain boundaries on the surface with chemical phase heterogeneity. Most TMs within the particle reach their highest charged state at 4.4 V even with the 0.1 C charging rate. However, multiheterogenous oxidation domains are still widely distributed at 4.6 V. Although no obvious further oxidation of TMs can be observed from X-ray absorption spectrometry (XAS) once the voltage reaches 4.4 V (refs. 9,31), dynamic charge compensation continues within the particle as the voltage increases further, beyond the anion activation plateau. These findings indicate that non-uniform charge transfer is hard to inhibit even at slow reaction rates. At the end of the charging process (4.8 V), cobalt undergoes oxidization uniformly throughout the particle, whereas a hierarchical reduction of manganese and nickel appears on the surface, which is correlated with irreversible oxygen release[32,33]. Both TM cations and oxygen anions experience heterogeneous electrochemical reactions, but the oxidation pattern of O^{2-} demonstrates a close relationship with particle geometry and size. There is an obvious valence-state gradient from the surface to the deeper bulk (Supplementary Figs. 21 and 22), which may contribute to the observed thickness dependence. The outer layer of more highly oxidized oxygen anions exhibits stronger chemical diffusivity and is thus responsible for the oxygen release on the particle surface. Meanwhile, the inner parts may undergo further partial transformation or activation in the form of trapped oxygen or peroxo-like species in the subsequent cycles[20], as indicated by the oxygen-poor segments in Fig. 2a. The inward growth of highly oxidized oxygen and reduced manganese/nickel at the same location provide strong evidence of the structural degradation mechanism. TM migration is considered to be one of the consequences related to oxygen release, and is coupled with transformation from Mn^{4+} to Mn^{3+} on the surface. In addition, for the outer layer of the particle, the mapping of the 2D valence state and 3D composition indicates the correlation between phase and valence state. In the bulk volume of large thicknesses, such correlation exhibits a different pattern due to the dimensional difference of these two methods. For the 3D chemical composition, a voxel represents the element information for a volume of 25 nm^3 (Supplementary Fig. 23b). In contrast, a pixel in the 2D valence state mapping represents the effective state along the thickness direction (Supplementary Fig. 23c).

During the discharging process, structural rearrangement induces Jahn–Teller distortion and stimulates the disproportionation reaction[34]. Interestingly, besides the reduced manganese on the surface, we also notice a small area of nanodomains in which $Mn^{2.7+}$ and $Ni^{3.4+}$ coexist at the same location, indicating that the electron equilibrium of TMs on the particle surface may experience an alternative distortion route, leaving Ni^{4+} or a mixture of Mn^{4+} in the lattice and dissolved Mn^{2+} on the surface. Sporadically distributed oxidized oxygen could still be identified along the particle edge, which may be related to surface reconstruction progressing into the bulk, residual non-fully reduced oxygen due to the heterogeneous reaction, or the formation of a solid electrolyte interphase (SEI) layer via side reactions between extracted oxygen species and electrolyte[35]. These oxidation-state maps allow us to quantitatively evaluate or track redox reactions that occurred in the first cycle (as shown in Fig. 3b–e) and provide visible evidence that oxygen release dominates the irreversible phase transformation of this LRTMO.

Regarding the kinetically dependent charge-compensation mechanism, systemic analysis of the interplay of TM cations and oxygen anions is also performed by collecting the corresponding oxidation state mappings at 10 C and correlating these with the investigations on the evolution described above. During the initial charging process at different current densities (0.1 and 10 C), manganese in Fig. 3b remains approximately close to tetravalent in pristine material and throughout the charging process, and does not participate in charge compensation. However, the oxidation behaviour involving TM cations (cobalt and nickel shown in Fig. 3c,d) and oxygen anions (shown in Fig. 3e) contributes to the capacity, with substantial differences in the oxidation behaviour at different current densities. In a low-rate charging process, the oxidation of TMs mainly occurs below 4.6 V, while the oxidation of lattice oxygen predominates from 4.6 V to 4.8 V. However, in a high-rate charging process, the oxidation of TMs and lattice oxygen continues throughout the charging process up to 4.8 V. Upon charging to 4.8 V, cobalt and nickel undergo an effective oxidation, but their degree of oxidation is lower under high-rate conditions. There is a notable valence gradient for nickel and oxygen from the surface to the bulk when charged to 4.8 V. The oxidation state of nickel gradually decreases from the bulk to the surface, while the oxidation state of oxygen increases gradually, especially under the low-current-rate condition (0.1 C). The gradient distribution of the oxidation state of nickel and lattice oxygen along the particle radius can be attributed to the ligand-to-metal charge-transfer process, whereby lithium ions are extracted from the lattice, TMs are oxidized and electrons from the O 2*p* orbitals transfer to the Ni 3*d* orbitals, leading to a $3d^6 \rightarrow 3d^7\underline{L}$ charge-transfer process (where $\underline{L}$ represents a hole state in the O 2*p* band)[36]. As a result, long-lived Ni^{3+}/Ni^{4+} intermediates are formed at the surface, leading to lower-valence nickel and higher-valence lattice oxygen than in the bulk[8]. Oxidation of oxygen anions at the charging rate of 10 C results in a lower proportion of highly oxidized O^{2-} on the surface of the particle at 4.8 V. Therefore, the capacity contributed by oxygen-anion oxidation at high voltages is substantially limited.

Turning to the end of the discharge process, none of the elements involved in the redox process return to their initial oxidation state,

https://doi.org/10.1038/s41565-024-01773-4

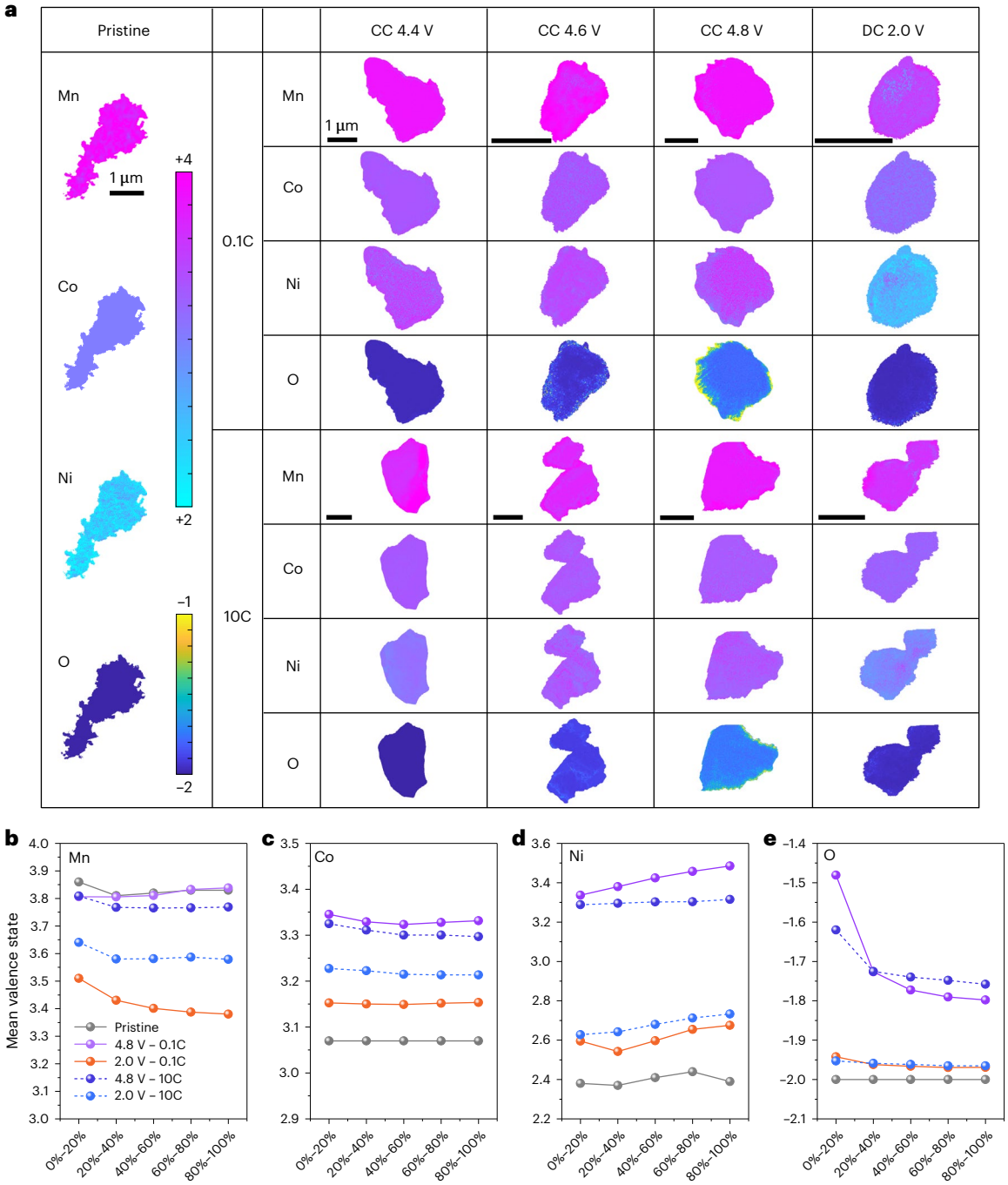

Fig. 3 | Oxidation state changes from spatial dependence to statistical analysis. a, The oxidation state mapping of manganese, cobalt, nickel and oxygen elements for the same particles shown in Fig. 2 at the representative SOCs in the initial cycle. The colour of each spot size was obtained by TXM, and the colour bar represents the valence state evolution of the corresponding elements calculated from fitting the linear combination with the reference spectra shown in Supplementary Fig. 20. **b**–**e**, The averaged gradient oxidation state of manganese (**b**), cobalt (**c**), nickel (**d**) and oxygen (**e**) for representative particles from the surface to the centre. The *x* axis corresponds to the equal-area regions in Supplementary Figs. 22 and 23. The sample is divided into five equal-area regions based on the 20% area increment from the outer boundary towards the centre, denoted as regions 0–20%, 20–40%, 40–60%, 60–80% and 80–100%, respectively.

resulting in the high degree of irreversibility shown in Fig. 1b. Although a small amount of surface manganese undergoes reduction to provide additional discharge capacity, nickel and cobalt reduction remains incomplete. A simple charge-balance calculation suggests that irreversible redox of nickel and cobalt needs to compensate for a capacity of 39 mAh g^{-1}, and the remaining irreversible capacity could be mainly attributed to the formation of new SEIs or other side reactions from the anode. Notably, the highly reversible reduction of oxygen anions suggests a limited impact of oxygen distortion on the redox properties. However, the sluggish reaction kinetics and the heterogeneous charge compensation play increasingly important roles as the number of cycles increases, and are associated with inhomogeneous dynamics of lithium ions, leading to increasing internal strain. Therefore, the distribution of highly irreversible valence states and the formation of aggregated lithium ions are responsible for a lower ICE of the LRTMO at high current rate, and the further accumulated strain intensifies the extent of structural degradation although less layer-to-spinel phase transformation occurs on the particle surface (Fig. 1f).

https://doi.org/10.1038/s41565-024-01773-4

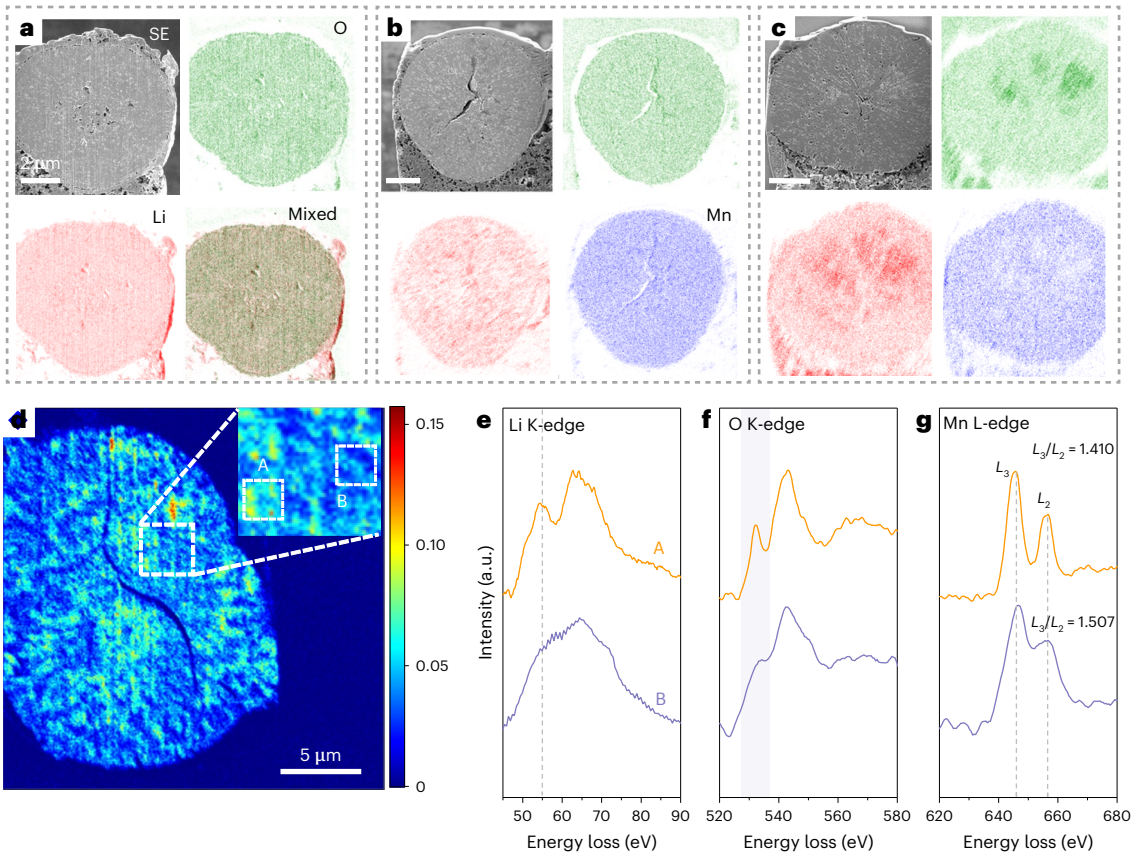

Fig. 4 | Elemental distribution and local environments. a–c, FIB-SEM secondary electron cross-sectional image (grey) and TOF-SIMS maps of the normalized elemental distribution for ^{7}Li (red) and ^{16}O (green) in pristine, ^{7}Li (red), ^{55}Mn (blue) and ^{16}O (green) (**a**), charged to 4.8 V for 20 cycles with the currents of 0.1 C (**b**) and 10 C (**c**). **d–g**, TOF-SIMS map of the normalized ^{16}O distribution for the cross section of LRTMO after 20 cycles at 4.8 V with a current of 10 C (**d**), and the corresponding EELS Li K-edge (**e**), O K-edge (**f**) and Mn L-edge (**g**) spectra of O-rich and non-O-rich areas (A, O-rich region; B, non-O-rich region).

In the sample degraded at 0.1 C for 20 cycles, the capacity contribution from manganese and cobalt increases and the capacity contribution from nickel decreases compared with the first cycle. For the sample degraded at 10 C, the redox activity of TMs decreases due to the accumulation of lattice distortions. The feature at 523–524 eV emission energy and 531–532 eV excitation energy from mRIXS (Supplementary Fig. 24b,c) appears when charging to 4.8 V and disappears when discharging to 2.0 V, indicating that oxygen redox activities are still well maintained after 20 cycles for cycling at both 0.1 C and 10 C.

Initiation and growth of tensile strain

Figure 4a–c demonstrates the ionic distribution of lithium ions and oxygen anions in the particle by time-of-flight secondary ion mass spectrometry (TOF-SIMS). The cross-sectional image of the pristine sample exhibits compacted void structures at the core, which are formed during the synthesis process. TOF-SIMS quantitative analysis reveals that lithium ions and oxygen anions are uniformly distributed throughout the particle in the pristine state. Supplementary Fig. 26a (4.8 V in the first cycle) and Fig. 4b (4.8 V in the 20th cycle) demonstrate that manganese cations and oxygen anions remain almost homogeneously distributed throughout the particle when cycling at 0.1 C, except for topographic-effect-related intensity differences at crack edges[37]. These findings suggest that only slight manganese dissolution occurred in the bulk area. The observed heterogeneous oxygen loss throughout the particle is consistent with the soft TXM observation of an oxygen-poor area (Fig. 2a) at high voltages. Because gas is evolved as a result of chemical diffusion of oxygen defects in the bulk, which directly leads to the formation of nano- to microsized pores, the stress level and elemental occupations are easily changed, creating and stimulating cracks at multiple uneven points during subsequent cycles. In addition, Fig. 4b shows clear evidence that large amounts of lithium ions are extracted from the host structure in the fully charged state, resulting in a non-uniform lithium-ion distribution even at 0.1 C. The adjacent domains become more pronounced after 20 cycles.

Lithium, oxygen and manganese demonstrate inhomogeneous distribution patterns when cycled at 10 C (Fig. 4c and Supplementary Fig. 26b), consistent with the chemical heterogeneities shown in Fig. 2a. Inhomogeneous lithium aggregation could be clearly identified, but the distribution pattern does not follow Fick's first law[38] to form a concentration gradient along the diffusion pathway. Lithium heterogeneity is already formed within the initial cycle at 10 C (Supplementary Fig. 26b), which is related to internal inhomogeneous dynamic lithium-ion diffusion. The lithium-site transformation aggravates the accumulation of residual 'trapped' lithium within the host structure, in agreement with NPD characterizations of the electrode after 20 cycles (Supplementary Fig. 3b). Fewer lithium ions can be reversibly deintercalated and form lithium-rich regions during fast cycling. In addition, these regions partly overlap with oxygen-enriched areas, which can be associated with a higher proportion of oxygen distortion or lithium–oxygen intraformational sliding. Furthermore, the large oxygen-rich areas also cover regions with lower concentrations of manganese, contributing to manganese-ion dislocation and dissolution[22]. EELS spectral analysis (Fig. 4e–g) focused on two representative regions in the TOF-SIMS maps (Fig. 4d), where oxygen-rich domains could be easily identified. The pre-edge peaks in the Li K-edge spectrum are highly sensitive to local lithium-ion occupancy and migration between different sites. In addition, the intensity is found to be strongly

https://doi.org/10.1038/s41565-024-01773-4

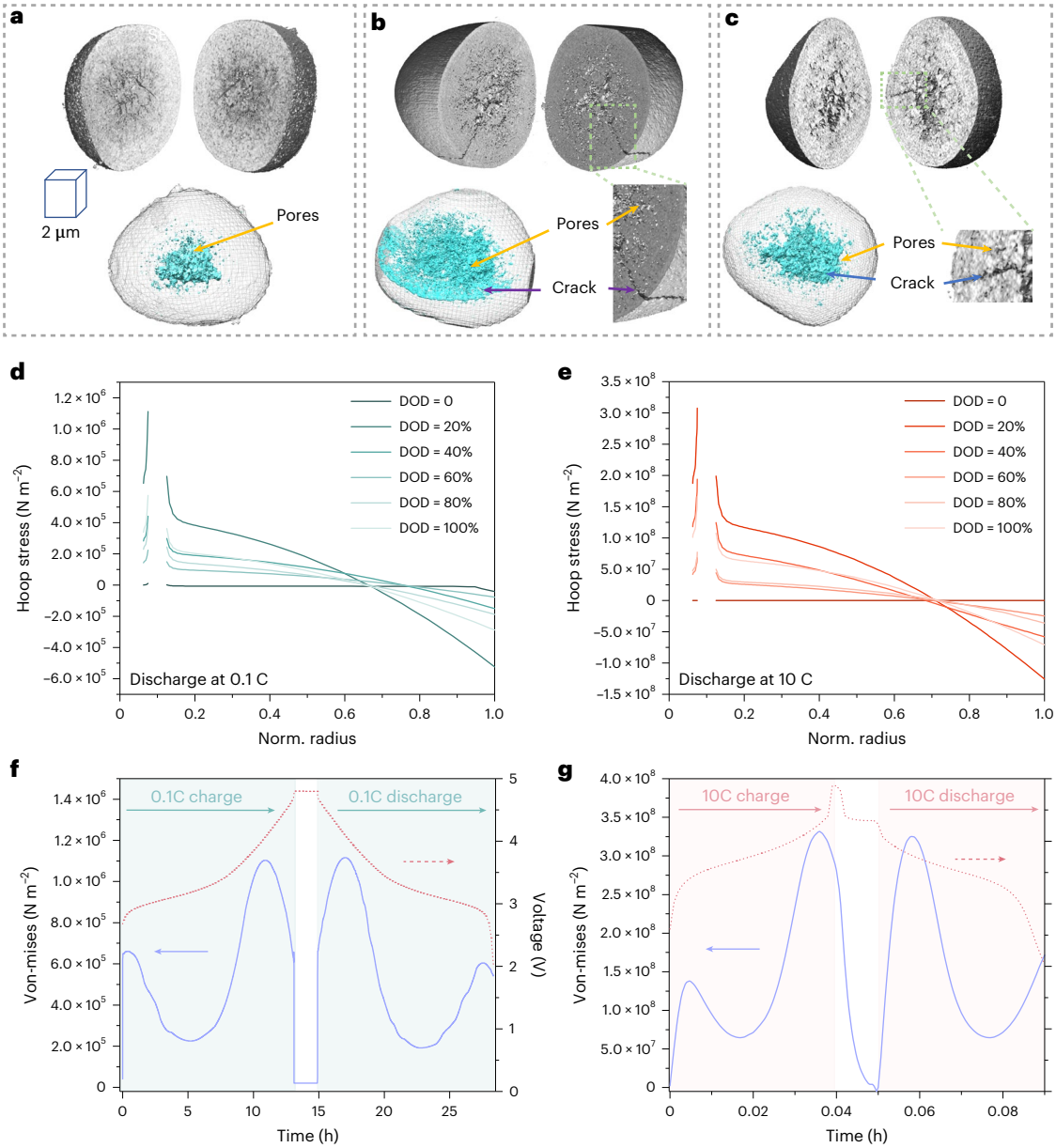

Fig. 5 | Particle nanotomography and complementary modelling of the microstructure. a–**c**, Visualizations of the internal isolated pores and interconnected crack network are highlighted (in cyan) within the reconstructed particle for pristine material (**a**), and for material degraded at 0.1 C (**b**) and 10 C (**c**). **d**–**g**, Evolution of hoop stress along the radial direction with DOD at 0.1 C (**d**) and 10 C (**e**), and von Mises stress during the charging–discharging processes at 0.1 C (**f**) and 10 C (**g**). The simulation of a single LRTMO particle (r = 8 µm) with a simplified central spherical void (r = 0.5 µm) and outer pores (r = 0.2 µm) in the lithium-ion flux streamlines is shown in Supplementary Fig. 27, which couples the lithium-ion diffusion with solid mechanics to predict stress evolution within the particle during the delithiation process, including the distribution of lithium-ion concentrations, von Mises stress at the bridge point A (as shown in Supplementary Fig. 28) between a central void and a neighbouring pore.

dependent on lithium-ion concentration[39]. The pre-peak intensity differences agree well with the quantification of local lithium atoms for the selected regions as shown by TOF-SIMS mapping. Features in the O K-edge spectrum correspond to the fine structure of the coordinated environment, especially the pre-peak at 530 eV arising from the hybridization of O 2*p* with TM 3*d* orbitals[40] and local lithium amount[41]. Oxygen distortion alters the TM–oxygen distance and strongly influences the lithium-ion diffusion. Although the lower intensity of the pre-edge feature indicates the presence of more electrons occupying the TM 3*d* orbitals, the lower number of lithium ions in region B leads to a higher manganese valence state in the system than that seen in oxygen-rich domains. Therefore, the structural evolution is inconsistent with the regular layer to spinel phase transition behaviour[4].

The 3D full-field transmission X-ray phase-contrast nanotomography shown in Fig. 5a proves the existence of a compact void structure at the core, whereas the samples cycled at different rates show two forms of internal pore volume. As depicted in Fig. 5b, a higher proportion of void space can be observed within the particle when the electrode is cycled at 0.1 C, which could be formed by the accumulation of released oxygen gas. A visible crack propagates through the nano- and micropores with a distribution gradient along the radial direction. Fewer, but larger, irregularly shaped pores can be observed in the 10 C sample (Fig. 5c). The pores are interconnected and developed with the spreading of cracks through the particles. The cracks can be clearly observed on particles cycled at different currents, but are probably developed by two formation routes. Modelling of the

stress distribution (Supplementary Fig. 27) is illustrated in Fig. 5d,e: the depth-of-discharge (DOD) progress leads to a notable tensile of hoop stress occurring at the bridge point A (Supplementary Fig. 28), which makes the crack prone to nucleate in the internal void area from the inside. Although a higher number of pores distributed within the material cycled at 0.1 C is observed, the stress at the internal void area of the high-rate-cycling sample is even greater. The hoop stress reaches up to 3.17×10^8 N m^{-2} when discharged at 10 C with 20% DOD, which is at least two orders of magnitude higher than an electrode discharged at 0.1 C to the same DOD stage. Furthermore, calculation of the von Mises stress (Fig. 5f,g) demonstrates that lithium-ion insertion–extraction induces a large volume change, and the particle would experience a dramatic variation depending on the stress concentration, particularly for the case of high-rate cycling. Heterogenous lithium-ion diffusion and non-uniform lattice distortion at high current rates increases the possibility of crack initiation and accelerates the crack growth rate through the particle.

Conclusion

In essence, soft TXM makes it possible to visualize consolidated chemical states in LRTMO particles with high spatial resolution and helps to reveal insights into heterogeneous chemical reactions at representative SOCs during the electrochemical cycling process in terms of morphology, chemistry, structure and oxidation state. Substantial oxygen defects and oxygen distortions are identified at different charging rates in the first cycle, which represent distinct degradation pathways of the LRTMO. Oxygen defects occur during the slow electrochemical process, dominating degradation in the form of lattice structure transformation and nanovoid injection. Oxygen release at the surface and local diffusion in the bulk are mainly responsible for voltage decay. In sharp contrast, in the case of oxygen-defect-driven degradation, the primary cause of capacity fading at fast cycling rates is the accumulation of lattice displacement/strain and limited ionic diffusion. Kinetic and dynamic effects are found to be the main factors determining degradation pathways. Thus, strategies to inhibit degradation of LRTMOs should focus on the reaction homogeneity, lattice stability and ionic diffusivity in the host structure. The insights in this study will inspire new thoughts for designing high-performance cathodes with stable and efficient cationic and anionic redox processes.

Online content

Any methods, additional references, Nature Portfolio reporting summaries, source data, extended data, supplementary information, acknowledgements, peer review information; details of author contributions and competing interests; and statements of data and code availability are available at https://doi.org/10.1038/s41565-024-01773-4.

References

1. Wang, J. et al. Lithium- and manganese-rich oxide cathode materials for high-energy lithium ion batteries. *Adv. Energy Mater.* **6**, 1600906 (2016).
2. Nayak, P. K. et al. Review on challenges and recent advances in the electrochemical performance of high capacity Li- and Mn-rich cathode materials for Li-ion batteries. *Adv. Energy Mater.* **8**, 1702397 (2018).
3. Hy, S., Liu, H., Zhang, M., Qian, D. & Hwang, B. Performance and design considerations for lithium excess layered oxide positive electrode materials for lithium ion batteries. *Energy Environ. Sci.* **9**, 1931–1954 (2016).
4. Zuo, W. et al. Li-rich cathodes for rechargeable Li-based batteries: reaction mechanisms and advanced characterization techniques. *Energy Environ. Sci.* **13**, 4450–4497 (2020).
5. Assat, G. et al. Fundamental interplay between anionic/cationic redox governing the kinetics and thermodynamics of lithium-rich cathodes. *Nat. Commun.* **8**, 2219 (2017).
6. Liu, T. et al. Origin of structural degradation in Li-rich layered oxide cathode. *Nature* **606**, 305–312 (2022).
7. Huang, J. et al. Non-topotactic reactions enable high rate capability in Li-rich cathode materials. *Nat. Energy* **6**, 706–714 (2021).
8. Hong, J. et al. Metal–oxygen decoordination stabilizes anion redox in Li-rich oxides. *Nat. Mater.* **18**, 256–265 (2019).
9. He, X. et al. Chemical and structural evolutions of Li–Mn-rich layered electrodes at different current densities. *Energy Environ. Sci.* **15**, 4137–4147 (2022).
10. Lin, F. et al. Metal segregation in hierarchically structured cathode materials for high-energy lithium batteries. *Nat. Energy* **1**, 15004 (2016).
11. Xu, Y. et al. In situ visualization of state-of-charge heterogeneity within a $LiCoO_2$ particle that evolves upon cycling at different rates. *ACS Energy Lett.* **2**, 1240–1245 (2017).
12. Sorrentino, A. et al. Soft X-ray transmission microscopy on lithium-rich layered-oxide cathode materials. *Appl. Sci.* **11**, 2791 (2021).
13. Wang, L. et al. Reaction inhomogeneity coupling with metal rearrangement triggers electrochemical degradation in lithium-rich layered cathode. *Nat. Commun.* **12**, 5370 (2021).
14. Shapiro, D. A. et al. Chemical composition mapping with nanometre resolution by soft X-ray microscopy. *Nat. Photonics* **8**, 765–769 (2014).
15. Yu, Y. S. et al. Three-dimensional localization of nanoscale battery reactions using soft X-ray tomography. *Nat. Commun.* **9**, 921 (2018).
16. Yang, Y. et al. Quantification of heterogeneous degradation in Li-ion batteries. *Adv. Energy Mater.* **9**, 1900674 (2019).
17. Zheng, J. et al. Structural and chemical evolution of Li- and Mn-rich layered cathode material. *Chem. Mater.* **27**, 1381–1390 (2015).
18. Yan, P. et al. Injection of oxygen vacancies in the bulk lattice of layered cathodes. *Nat. Nanotechnol.* **14**, 602–608 (2019).
19. House, R. A. et al. First-cycle voltage hysteresis in Li-rich 3*d* cathodes associated with molecular O_2 trapped in the bulk. *Nat. Energy* **5**, 777–785 (2020).
20. House, R. A. et al. The role of O_2 in O-redox cathodes for Li-ion batteries. *Nat. Energy* **6**, 781–789 (2021).
21. Zhou, Y. N. et al. High-rate charging induced intermediate phases and structural changes of layer-structured cathode for lithium-ion batteries. *Adv. Energy Mater.* **6**, 1600597 (2016).
22. Sharifi-Asl, S. et al. Revealing grain-boundary-induced degradation mechanisms in Li-rich cathode materials. *Nano Lett.* **20**, 1208–1217 (2020).
23. Xu, B., Fell, C. R., Chi, M. & Meng, Y. S. Identifying surface structural changes in layered Li-excess nickel manganese oxides in high voltage lithium ion batteries: a joint experimental and theoretical study. *Energy Environ. Sci.* **4**, 2223–2233 (2011).
24. Zhong, J. et al. Mitigating evolution of lattice oxygen and stabilizing structure of lithium-rich oxides by fabricating surface oxygen defects. *Electrochim. Acta* **328**, 134987 (2019).
25. Csernica, P. M. et al. Persistent and partially mobile oxygen vacancies in Li-rich layered oxides. *Nat. Energy* **6**, 642–652 (2021).
26. Mohanty, D. et al. Unraveling the voltage-fade mechanism in high-energy-density lithium-ion batteries: origin of the tetrahedral cations for spinel conversion. *Chem. Mater.* **26**, 6272–6280 (2014).
27. Liu, X. et al. Origin and regulation of oxygen redox instability in high-voltage battery cathodes. *Nat. Energy* **7**, 808–817 (2022).
28. Qiu, B. et al. Gas–solid interfacial modification of oxygen activity in layered oxide cathodes for lithium-ion batteries. *Nat. Commun.* **7**, 12108 (2016).
29. Kawai, K. et al. Kinetic square scheme in oxygen-redox battery electrodes. *Energy Environ. Sci.* **15**, 2591–2600 (2022).

30. Guttmann, P. et al. Nanoscale spectroscopy with polarized X-rays by NEXAFS-TXM. *Nat. Photonics* **6**, 25–29 (2012).
31. Yu, X. et al. Understanding the rate capability of high-energy-density Li-rich layered $Li_{1.2}Ni_{0.15}Co_{0.1}Mn_{0.55}O_2$ cathode materials. *Adv. Energy Mater.* **4**, 1300950 (2014).
32. Li, Q. et al. Improving the oxygen redox reversibility of Li-rich battery cathode materials via Coulombic repulsive interactions strategy. *Nat. Commun.* **13**, 1123 (2022).
33. Li, N. et al. Unraveling the cationic and anionic redox reactions in a conventional layered oxide cathode. *ACS Energy Lett.* **4**, 2836–2842 (2019).
34. Sun, T. et al. Soft X-ray ptychography chemical imaging of degradation in a composite surface-reconstructed Li-rich cathode. *ACS Nano* **15**, 1475–1485 (2021).
35. He, W. et al. Challenges and recent advances in high capacity Li-rich cathode materials for high energy density lithium-ion batteries. *Adv. Mater.* **33**, 2005937 (2021).
36. Yoon, W. S. et al. Investigation of the charge compensation mechanism on the electrochemically Li-ion deintercalated $Li_{1-x}Co_{1/3}Ni_{1/3}Mn_{1/3}O_2$ electrode system by combination of soft and hard X-ray absorption spectroscopy. *J. Am. Chem. Soc.* **127**, 17479–17487 (2005).
37. Bessette, S. et al. Nanoscale lithium quantification in $Li_xNi_yCo_wMn_zO_2$ as cathode for rechargeable batteries. *Sci. Rep.* **8**, 17575 (2018).
38. Ruess, R. et al. Influence of NCM particle cracking on kinetics of lithium-ion batteries with liquid or solid electrolyte. *J. Electrochem. Soc.* **167**, 100532 (2020).
39. Zhang, W. et al. Kinetic pathways of ionic transport in fast-charging lithium titanate. *Science* **367**, 1030–1034 (2020).
40. Hu, E. et al. Evolution of redox couples in Li- and Mn-rich cathode materials and mitigation of voltage fade by reducing oxygen release. *Nat. Energy* **3**, 690–698 (2018).
41. Kikkawa, J. et al. Chemical states of overcharged $LiCoO_2$ particle surfaces and interiors observed using electron energy-loss spectroscopy. *J. Phys. Chem. C* **119**, 15823–15830 (2015).

[1]School of Chemical Engineering, Sichuan University, Chengdu, China. [2]School of Microelectronics, Southern University of Science and Technology, Shenzhen, China. [3]Energy Storage & Distributed Resources Division, Lawrence Berkeley National Laboratory, Berkeley, CA, USA. [4]Shenzhen Geim Graphene Center, Tsinghua–Berkeley Shenzhen Institute and Institute of Materials Research, Shenzhen International Graduate School, Tsinghua University, Shenzhen, China. [5]Department of Materials Science and Engineering, Shenzhen Key Laboratory of Full Spectral Solar Electricity Generation (FSSEG), Southern University of Science and Technology, Shenzhen, China. [6]X-Ray Microscopy Group at Helmholtz-Zentrum Berlin, Berlin, Germany. [7]Helmholtz-Institute Münster (HI MS), IEK-12, Forschungszentrum Jülich GmbH, and MEET Battery Research Center, University of Münster, Münster, Germany. [8]ESRF—The European Synchrotron Radiation Facility, Grenoble, France. [9]National Synchrotron Light Source II, Brookhaven National Laboratory, Upton, NY, USA. [10]College of Chemical and Biological Engineering, Zhejiang University, Hangzhou, China. [11]Institute of Advanced Science Facilities, Shenzhen, China. [12]Department of Energy, Politecnico di Milano, Milan, Italy. [13]College of Electrical Engineering, Sichuan University, Chengdu, China. [14]These authors contributed equally: Zhimeng Liu, Yuqiang Zeng, Junyang Tan, Hailong Wang. ✉e-mail: junzoelu@zju.edu.cn; jie1.li@polimi.it; linyj2020@sustech.edu.cn; xinhe@scu.edu.cn

Methods

Material synthesis

The LRTMO ($Li_{1.2}Mn_{0.56}Ni_{0.16}Co_{0.08}O_2$) was prepared by a continuous stirring/coprecipitation method followed by a high-temperature annealing process. A mixed solution of Li_2CO_3 and NH_4OH was pumped into a mixed solution of dissolved $NiSO_4{\cdot}6H_2O$, $CoSO_4{\cdot}7H_2O$ and $MnSO_4{\cdot}4H_2O$ (2:1:7, mol/mol/mol) in a tank reactor (CSTR) at 25 °C. The precipitate was washed several times with distilled water and dried in a vacuum oven at 100 °C for over 12 h. Then, stoichiometric amounts of $(Ni_{0.2}Co_{0.1}Mn_{0.7})CO_3$ precipitate and Li_2CO_3 were thoroughly mixed to form the precursor powder. This was first heated at 500 °C for 5 h and then annealed at 850 °C in air for 15 h; the LRTMO was obtained after the powder was allowed to cool naturally to room temperature.

Electrode preparation and electrochemical measurements

Electrodes were prepared by casting a slurry with the composition of 80 wt% LRTMO active material, 10 wt% Super C65 and 10 wt% polyvinylidene difluoride on aluminium foil. The slurry used to prepare electrode samples was made by a magnetic stirring process. The electrodes were tested with two-electrode T-cells which consisted of an LRTMO electrode in contact with preactivated lithium foil; 60 µl 1 M $LiPF_6$ in 1:1 (wt%) ethylene carbonate/dimethyl carbonate was added as electrolyte. The lithium foil was first electrodeposited in a symmetric cell at 0.2 mA cm^{-2} for 5 h to reduce the influence of SEI[42] formation on the lithium. The cells were suspended and disassembled at representative SOCs. After being washed twice with dimethyl carbonate, the electrodes were dried at 60 °C under vacuum and then kept in an argon atmosphere for further measurements.

Materials characterization

Nanoresolution X-ray spectromicroscopy. Soft X-ray spectromicroscopy was conducted to scan LRTMO particles at different electrochemical states in the undulator beamline U41-XM at the BESSY II synchrotron (Helmholtz-Zentrum Berlin für Materialien und Energie, Germany). The samples were selected from particles located on the top surface of electrode and then loaded on a TEM grid enabling rotation with an angular increment step size of 1° at a pixel size of 9.8 nm (25 nm zone plate objective) for soft X-ray nanotomography. A schematic illustration of the soft TXM system is shown in Supplementary Fig. 21a. To achieve sufficient transparency to soft X-rays and preserve the secondary structure of the LRTMO, material was slowly milled to reduce the particle size for further characterization. The sample is located between the X-ray source and the detector. Then the X-ray source and detector rotate around the sample to collect projected images for the oxygen, manganese, cobalt and nickel elements at each angle. All the samples were measured at two specific photon energies (Supplementary Table 1) to resolve the distribution of each element at the same angle. The projected images of selected samples were started at a tilt angle of 0° and then turned to ±65°. Finally, the 3D spatial distribution of the chemical composition is obtained by reconstructing all these 2D projection images through software (Avizo) while the 2D slice is extracted from slicing the 3D reconstructed volume. The irradiation dose was set to prevent structural information loss due to irreversible radiation damage. A schematic diagram of the dual-energy multiangle tomographic data set acquisition and 3D chemical composition reconstruction process are shown in Supplementary Fig. 21b. In this work, a deviation of 5.0% was used to differentiate the phases for all the elements based on the statistical results. Specifically, the 3D chemical composition is computed for each voxel of 25 nm^3 (spatial resolution) with the measured absorption at each pixel and X-ray photon energy. Based on the reconstructed 3D chemical distribution, the element segmentation of the particles was processed automatically and the variation in the stoichiometric ratio compared to that of the original composition.

Reconstruction and segmentation. The oxidation-state mapping of the same samples was measured by matching the absorption spectrum at each pixel to the standard element oxidation states (Supplementary Table 2) to quantify the projected oxidation-state mapping of the selected element. We obtained the absorption spectrum across a certain range of energies (Supplementary Table 2) for each sample. Based on the reference spectra of each element (Supplementary Fig. 20), the energy range of interest is 526–536 eV, 638–648 eV, 775–782 eV and 850–860 eV for oxygen, manganese, cobalt and nickel, respectively. In the experiments, a broad energy range was used, that is, 525–555 eV, 635–665 eV, 775–805 eV and 848-880 eV for oxygen, manganese, cobalt and nickel, respectively. Each spectrum was fitted with a linear combination of the associated reference spectra (Supplementary Fig. 20). The extracted fit coefficients indicate the contribution of each standard valence state, and thus the effective state can be determined as a combination of standard states. A schematic diagram of 2D oxidation-state mapping data acquisition is shown in Supplementary Fig. 21c.

X-ray phase-contrast tomography. Full-field transmission X-ray nanotomography based on phase contrast with high spatial resolution (voxel value, 20 nm) was conducted at the ID16A-NI nanoimaging beamline of the European Synchrotron Radiation Facility (ESRF), Grenoble, France. The holotomography measurements offer a unique nanofocus with very high photon flux (up to 10^{12} photons s^{-1} at $\Delta E/E \approx 1\%$). The free space in the particle allows propagation of the X-ray beam. The contrast in the images is dominated by phase contrast, related to the real part of the complex refractive index, which is determined by the electron density of corresponding material. The sample particle was placed downstream of the Kirkpatrick–Baez focus and magnified radiographs were recorded onto an X-ray detector using the FReLoN charged-coupled device camera with a 2048 × 2048 binned pixels array. The 2D phase maps are retrieved from the angular projections and then used as input for 3D tomographic reconstruction based on the filtered back-projection algorithm method (ESRF PyHST software package).

sXAS and mRIXS measurements. Soft XAS and mRIXS measurements were carried out at the Advanced Light Source (ALS) in Lawrence Berkeley National Laboratory (LBNL). The nickel, cobalt and managanese L-edge spectra were collected at room temperature under an ultrahigh vacuum (10^{-9} yorr) measuring total electron yield via the drain current, and total fluorescence yield via silicon photodiodes. The spectra were normalized to the beam flux and resolution of the excitation energy was 0.15 eV. The mRIXS maps were acquired after energy calibration and normalization, and mRIXS–super-partial fluorescence yield profiles were obtained after integrating the mRIXS intensity in the range of emission energy from 523 to 524 eV. Further analysis details have been reported previously[43].

NPD. NPD results were collected at the VULCAN instrument at Oak Ridge National Laboratory. The powder sample was collected from the electrode and then loaded into a vanadium sample can in a glovebox. An incident beam (5 mm × 12 mm) of 0.7–3.5 Å bandwidth, allowing 0.5–2.5 Å d-space in the diffracted pattern of the ±90° 2θ detector banks, was selected using double-disk choppers at 30 Hz frequency. A high-resolution mode was employed with $\Delta d/d \approx 0.25\%$. NPD data were collected in high-resolution mode for a duration of 3 h and processed using VDRIVE software. The data were normalized to a vanadium rod. Rietveld refinement of the neutron diffraction data was performed using GSAS software with the EXPGUI interface.

TOF-SIMS measurements. Cross sections of cycled cathodes were prepared by focused ion beam (FIB) SEM on a TESCAN Amber microscope, which was also used to perform the TOF-SIMS. The FIB column provides the primary ion source for the TOF-SIMS technique: the bombardment of gallium ions on the sample surface, and the resulting

collision cascade, will eject surface atoms. The ejected atoms, called secondary species, can be neutrons, electrons, molecules or ions. The ionized particles (single elements or molecules) produced secondary ions that were collected in the mass analyser by applying a potential difference. An area of 17.2 × 17.2 μm^2 was analysed using gallium ions with 30 keV energy and 11 pA current.

STEM measurement. Cross-sectional TEM specimens were prepared by FIB cutting (FEI Helios 600i). To protect the sample, the region of interest is locally capped in the FIB with electron-beam-deposited platinum and then ion-beam-deposited amorphous carbon. The major milling is done with a 30 kV gallium ion beam while the milling progress is controlled with the SEM system. Final milling to minimize the damage layer on the specimens is performed with 2 kV gallium ion beam. The typical TEM specimen thickness is ~50 nm. To investigate the structural evolution differences with different current rates, cross-sectional STEM samples were used to directly probe the local atomic structure along the [010] zone axes. HAADF and iDPC images were obtained on a cold-field-emission spherical-aberration-corrected transmission electron microscope (FEI Spectra 300) operating at 300 kV. To resolve the structure of electrode materials, a low electron dose rate of around 35 e Å^{-2} s^{-1} was used for imaging to reduce the possible structural damage from the electron beams. The collective semiangles of HAADF and iDPC were 62–200 mrad and 7–29 mrad, respectively.

EELS. EELS spectra were acquired using a Titan Themis G2 60-300 in STEM mode. Dual EELS was used to collect both the low-loss and high-loss spectra, and the low-loss spectra were utilized to correct the drift of the zero-loss peak. Based on the full-width at half-maximum of the zero-loss peak, the optimal energy resolution of EELS is about 4.7 eV. The EELS data were analysed and processed with Gatan3.0 software.

Operando XRD. The operando XRD measurements for the first cycle at 0.1 C were performed using a laboratory-based X-ray diffractometer (DX-2800, Haoyuan Instrument), with Cu Kα radiation (λ = 1.54186 Å) and a silicon drift detector. To ensure a high rate of measurement, every scan was collected in 0.02° increments between 15° and 40° at a scanning speed of 1° min^{-1}. A specially designed coin-type cell with X-ray-transparent windows sealed with aluminium films was used for the laboratory XRD test.

The operando XRD measurements for the first cycle at 10 C were performed with the Liquid Metal Jet Source (using Ga Kα radiation, 9.24 keV, λ = 1.3418 Å) at the Institute of Advanced Science Facilities, Shenzhen, China, with a Dectris Pilatus 1M detector in the 2θ range of 5°–58°. The exposure time for each pattern was 45 s to obtain a good signal-to-noise ratio. A specially designed coin-type cell with X-ray-transparent windows sealed with Kapton film was used for the fast XRD test.

Hard XAS measurement. The X-ray absorption near-edge spectroscopy and extended X-ray absorption fine structure spectroscopy measurements were carried out using a Rapid XAFS 1M laboratory X-ray absorption spectrometer (Anhui Absorption Spectroscopy Analysis Instrument) in transmission mode; Si(110), Si(533) and Si(551) spherically bent crystal analysers with a radius of curvature of 500 mm were used to acquire the manganse, cobalt and nickel XAS spectra, respectively.

Particle charge–discharge simulation

A simplified cell model is used to simulate the concentration distribution and diffusion-induced gravity distribution of lithium-rich particles with microsize voids in the centre during charging and discharging. The Faradaic current density (i), is responsible for Li^+ (de)intercalation on the lithium-rich particles and deposition/dissolution on lithium metal. The cathode is modelled through Butler–Volmer kinetics.

$$i = i_{0,\mathrm{ref}}\left(\exp\left(\frac{\alpha_a F\eta_c}{RT}\right) - \exp\left(\frac{-\alpha_c F\eta_c}{RT}\right)\right)$$

where i_0 is the exchange current density for the LRTMO cathode in our model $i_{0\_\mathrm{Li\text{-}rich}} = i_{0,\mathrm{ref}\_\mathrm{Li\text{-}rich}}$, $i_{0,\mathrm{ref}}$ is the reference exchange current density, α_a and α_c are the anode and cathode charge-transfer coefficient, respectively, F is the Faraday constant and η_c is the cathode overpotential.

The anode is modelled through lithium-metal kinetics.

$$i = i_{0,\mathrm{ref}}\left(\frac{C_l}{C_{l,\mathrm{ref}}}\right)^{\alpha_a}\left(\exp\left(\frac{\alpha_a F\eta_a}{RT}\right) - \exp\left(\frac{-\alpha_c F\eta_a}{RT}\right)\right)$$

where C_l is the electrolyte salt concentration, $C_{l,\mathrm{ref}}$ is the reference electrolyte salt concentration and η_a is the anode overpotential.

Lithium-ion transport in particles includes migration driven by an electric field and diffusion driven by the concentration gradient. The net flux density J_{Li} is the sum of two parts.

$$\nabla \cdot J_{Li} = R_{Li}$$

$$J_{Li} = -D_{Li}\nabla C_{Li} - z_{Li}u_{Li}FC_{Li}V$$

$$D_{Li} = 5 \times 10^{-13}\left(1{,}200\left(\frac{1}{T_{\mathrm{ref}}} - \frac{1}{T_2}\right)\right)$$

where the first term, representing diffusion kinetics, is the product of the diffusion coefficient D_{Li} and the gradient of the lithium-ion concentration; the second term, representing migration kinetics, is the product of the charge number z_{Li}, the mobility u_{Li} ($u = D_{Li}/RT$), the Faraday constant F, the lithium-ion concentration C_{Li} and the gradient of the electrolyte potential V. T_{ref} = 298 K, T_2 = min(393.15, max(T, 223.15)). A zero lithium-flux boundary condition is applied to the void surface inside the particle.

We assume that the cathode particles, binder and diaphragm are linearly elastic materials in the battery and that the internal stresses in the particles are mainly caused by the intercalation strain resulting from the lithium-ion deintercalation process.

In a geometrically non-linear context, the intercalation strain is represented by a deformation gradient,

$$F_{ic} = \left(1 + \frac{\Delta V}{V_0}\right)^{1/3} \cdot I$$

where ΔV is the change in cell volume due to deintercalation, V_0 is the pristine cell volume and I is the identity tensor.

$$V = a^2 \cdot b \cdot \sin\left(\frac{\pi}{3}\right)$$

$$\Delta V = V - V_0$$

The data for $\Delta V/V_0$ are taken from ref. 44.

The meanings and values of other parameters in the above equations are listed in Supplementary Table 3. The model is solved by the finite-element method implemented in COMSOL Multiphysics 6.0 assuming the system to be 2D axisymmetric.

Data availability

The source data underlying the main text figures (Figs. 1–5) and Supplementary Figs. 1–16, 19, 20, 24 and 25 are provided as source data files. Source data are provided with this paper.

References

42. He, X. et al. The passivity of lithium electrodes in liquid electrolytes for secondary batteries. *Nat. Rev. Mater.* **6**, 1036–1052 (2021).

43. Dai, K. et al. High reversibility of lattice oxygen redox quantified by direct bulk probes of both anionic and cationic redox reactions high reversibility of lattice oxygen redox quantified by direct bulk probes of both anionic and cationic redox reactions. *Joule* **3**, 518–541 (2019).
44. Liu, H. et al. Operando lithium dynamics in the Li-rich layered oxide cathode material via neutron diffraction. *Adv. Energy Mater.* **6**, 1502143 (2016).

Acknowledgements

We acknowledge the European Synchrotron Radiation Facility (ESRF) for provision of synchrotron radiation facilities under proposal number ma4084, and thank the Helmholtz-Zentrum Berlin fur Materialien und Energie for the allocation of synchrotron radiation beamtime, and support from TESCAN (Shanghai, China) for SEM-FIB and TOF-SIMS measurements. We are grateful for support from the Shenzhen Science and Technology Program (grant number RCYX20231211090432060 to Y.L.), the Sichuan Science and Technology Program (grant number 2023NSFSC1131 to Z.L.), the Shenzhen Stable Support Plan Program for Higher Education Institutions Research Program (grant number 20231120094333001 to Y. Zeng), and the Major Research Plan of the National Natural Science Foundation of China (grant number 92372207 to J. Lu and Y.X.).

Author contributions

X. He conceived and planned the project concept. J. Lu, J. Li, Y.L. and X. He supervised the project. Z.L. performed experiments and initial data analysis. Y. Zeng developed the deep analysis of the tomography data and reconstructed the 3D structure. J.T. and B.L. carried out STEM measurements and internal strain analyses. Y. Zhu and H.W. undertook the FIB preparation. H.W. performed TOF-SIMS analyses and stress simulations. X. Hou and X.G. performed NPD refinement. P.G. carried out soft TXM measurement. Y.Y. and P.C. carried out X-ray phase-contrast nanotomography and established the 3D reconstruction. D.Z. performed the rapid XRD measurements. Y.X., Y.W., M.W. and R.K. contributed to the scientific discussion of the data and revised the paper. All authors contributed to the interpretation, conclusions and preparation of the paper.

Competing interests

The authors declare no competing interests.

Additional information

Supplementary information The online version contains supplementary material available at https://doi.org/10.1038/s41565-024-01773-4.

Correspondence and requests for materials should be addressed to Jun Lu, Jie Li, Yuanjing Lin or Xin He.

Peer review information *Nature Nanotechnology* thanks Ke-Jin Zhou and the other, anonymous, reviewer(s) for their contribution to the peer review of this work.